ADVANCING EARTH AND SPACE SCIENCE

Geophysical Research Letters

RESEARCH LETTER
10.1029/2020GL090278

Key Points:

- We document a slow slip event on the Longitudinal Valley Fault (Taiwan) with magnitude of 5.45, which represents the largest detection to date
- Slow slip has likely been induced by a combination of coseismic and postseismic stress changes (>0.5 MPa) from the 2003 Chengkung mainshock
- Inherited state of stress on the fault has likely controlled the slip distribution and slip mode

Supporting Information:

- Supplementary Information S1

Correspondence to:
A. Canitano,
canitano@earth.sinica.edu.tw

Citation:
Canitano, A., Godano, M., & Thomas, M. Y. (2021). Inherited state of stress as a key factor controlling slip and slip mode: inference from the study of a slow slip event in the Longitudinal Valley, Taiwan. *Geophysical Research Letters*, *48*, e2020GL090278. https://doi.org/10.1029/2020GL090278

Received 10 AUG 2020
Accepted 14 DEC 2020

Inherited State of Stress as a Key Factor Controlling Slip and Slip Mode: Inference From the Study of a Slow Slip Event in the Longitudinal Valley, Taiwan

Alexandre Canitano[1], Maxime Godano[2], and Marion Y. Thomas[3]

[1]Institute of Earth Sciences, Academia Sinica, Nangang, Taipei, Taiwan, [2]Université Côte d'Azur, CNRS, Observatoire de la Côte d'Azur, IRD, Géoazur, Valbonne, France, [3]Sorbonne Université, CNRS-INSU, Institut des Sciences de la Terre Paris, ISTeP UMR 7193, Paris, France

Abstract Using borehole strainmeters, we detected a 13-day long slow slip event in 2011 with $M_w = 5.45$ on the Longitudinal Valley Fault, Taiwan. It has been likely promoted by the significant Coulomb stress changes (~0.5–1 MPa) imparted by a combination of coseismic and postseismic slip of the 2003 Chengkung earthquake. Using kinematic slip models, we infer that the slow event has accommodated about 15%–35% of the slip deficit accumulated from 1997 to 2011 in its source region. Further, we find that inherited state of stress may have controlled the slow event southward propagation. We also highlight a spatiotemporal correlation between the slow event and a cluster of repeating microearthquakes, suggesting a complex interplay between seismic and aseismic processes on the fault, where transient aseismic regions are adjacent to highly coupled zones.

Plain Language Summary Tectonic faults display a large range of slip behaviors, ranging from fast slip (earthquakes) to episodic or continuous aseismic slow slip. Episodic aseismic slip events (typically called 'slow slip events') are now widely observed in active regions and play an important role in stress redistribution in the Earth's crust. The Longitudinal Valley Fault is the most active fault in Taiwan, hosting large to destructive earthquakes. However, very little is known about the presence and the role of slow slip events on the fault deformation. We document a 13-day long slow slip event with a magnitude of 5.45, which represe'nts the largest event detected on the fault to date. We demonstrate that the slow event was likely encouraged by stress accumulation due to the 2003 Chengkung earthquake. Monitoring and characterizing the sources of aseismic slip is fundamental to identify areas with high seismic hazard on the fault and to shed some light on the interactions between seismic and aseismic processes.

1. Introduction

Over the last two decades, the growing development of geodetic and seismological monitoring arrays in active regions has revealed episodic aseismic slip in the crust, spanning timescales from seconds to years (e.g., Peng & Gomberg, 2010). These slow slip events (SSEs) play an important role in redistributing stress in the Earth's crust (e.g., Linde et al., 1996) and are now observed in various tectonic regions (e.g., Bürgmann, 2018). SSEs are often accompanied by earthquake swarms (Fasola et al., 2019; Gualandi et al., 2017; Vallée et al., 2013) or nonvolcanic tremors (e.g., Beroza & Ide, 2011), and together, represent an important mechanism of strain release in active regions. Therefore, investigating the stress conditions, the faulting mechanisms of slow slip and what role they play in the earthquake cycle is fundamental to determine time-dependent earthquake hazard.

In eastern Taiwan, the Longitudinal Valley (LV) is an active collision boundary between the Eurasian and Philippine Sea plates (Barrier & Angelier, 1986), and accounts for more than half of the 9 cm yr^{-1} of oblique plate convergence (Yu et al., 1997). The Longitudinal Valley Fault (LVF), which runs along the eastern side of the LV, represents the major active structure in the region and accounts for about 4.5 cm yr^{-1} of total plate convergence (Thomas, Avouac, Champenois, et al., 2014) (Figure 1). The fault is creeping at the surface at the rate of 1–6 cm/yr between latitudes 23°00′ and 23°30′ (Thomas, Avouac, Champenois, et al., 2014) and also experiences seasonal and transient creep episodes (Lee et al., 2003; Murase et al., 2013). Despite significant historical earthquakes, there is a paucity of large shocks along the fault relatively to the high convergence rate, suggesting that a significant fraction of the long-term slip rate, in the seismogenic depth range,

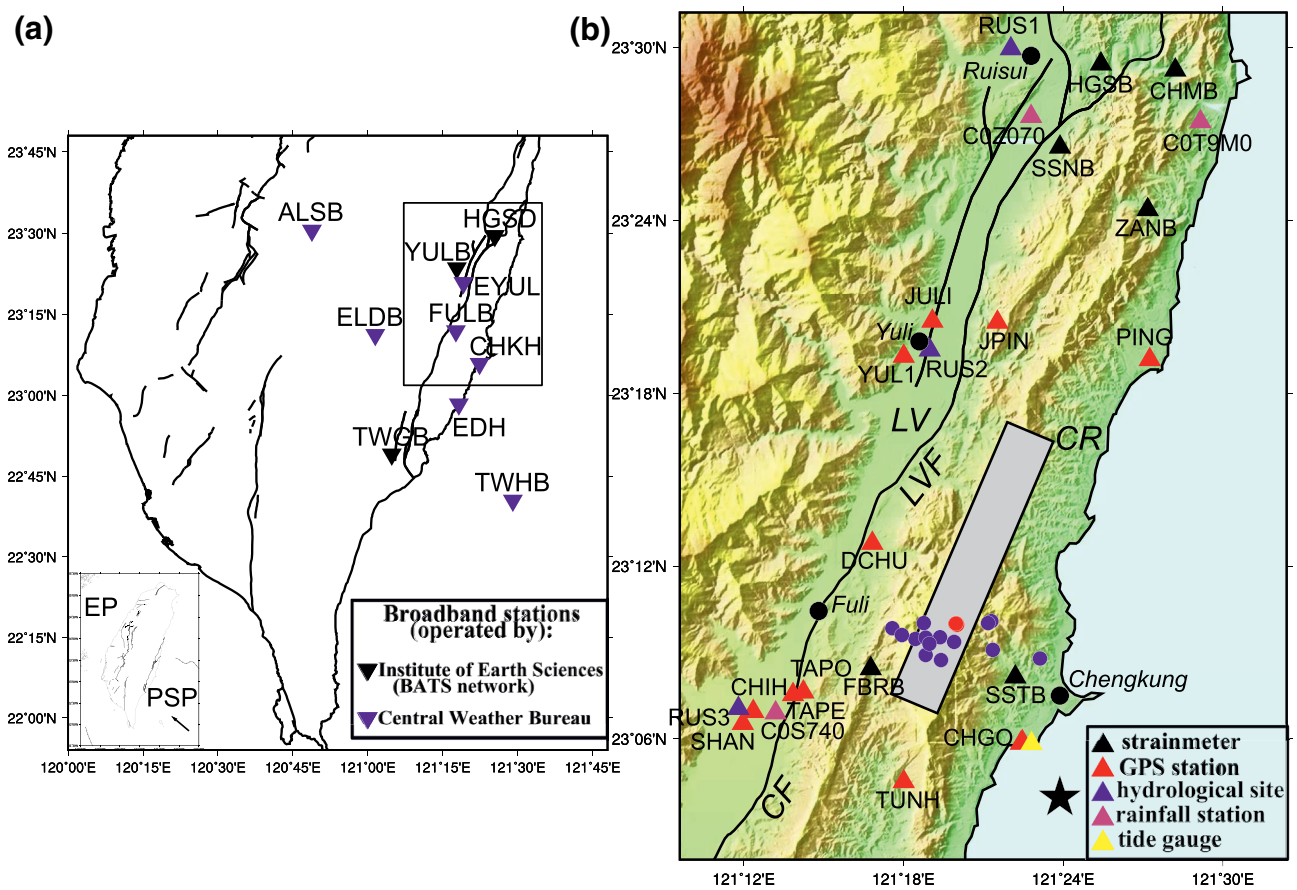

Figure 1. (a) Map of southern Taiwan. Inverted triangles denote broadband seismometers used in this study. (Inset) Geodynamic framework of Taiwan. Black arrow indicates relative motion between Philippine Sea plate (PSP) and Eurasian plate (EP). Black box shows the area in (b). (b) Map of the Longitudinal Valley. Gray rectangle indicates the surface projection of the SSE fault plane. Blue and red dots represent the earthquake multiplet before and after relocation, respectively (Section 4). Black star denotes the Chengkung earthquake epicenter and black dots the main towns. LV, Longitudinal Valley; CR, Coastal Range; LVF, Longitudinal Valley Fault, CF: Chihshang fault.

is released aseismically (Liu et al., 2009). Indeed, based on the analysis of geodetic data for the 1992–2010 period, Thomas, Avouac, Gratier, et al. (2014) demonstrate that 80%–90% of the long-term slip budget on the southern section of the LVF is the result of aseismic slip. Following the 2003 M_w 6.8 Chengkung earthquake, a 7-year long afterslip has been detected by Global Positioning System (GPS) stations along the Chihshang Fault (CF) (Thomas, Avouac, Champenois, et al., 2014), a 30-km long section of the southern LVF. Borehole strainmeters have captured a very shallow SSE (2–4 km depth) with geodetic moment magnitude $M_w \sim 4.5$ in central LV (Canitano et al., 2019). A 1-month long afterslip following a M_w 4.6 earthquake on the CF was also shown to control the rate of aftershocks near the earthquake source region (Canitano et al., 2018a). However, the dearth of aseismic transient observations in the region strongly limits our ability to investigate the mechanisms of slow deformation along the fault and to further interpret the interplay between seismic and aseismic processes.

In this study, we document a 2-week long SSE with an equivalent moment magnitude of 5.45. It occurred in January–February 2011 on the central section of the LVF, northeast of the source rupture of the 2003 Chengkung earthquake. This event occurred between about 8–14 km depth and was detected by borehole strainmeters deployed in two networks distant by 35 km. Using static Coulomb stress modeling, we investigate a possible contribution of coseismic and postseismic slip of the Chengkung event to the SSE occurrence. We also analyze the spatiotemporal pattern of a cluster of earthquake multiplets occurring during the SSE episode and investigate its relationship with aseismic slip. Finally, we investigate the behavior of the SSE region during the Chengkung earthquake and discuss the SSE contribution to the release of slip deficit along the LVF.

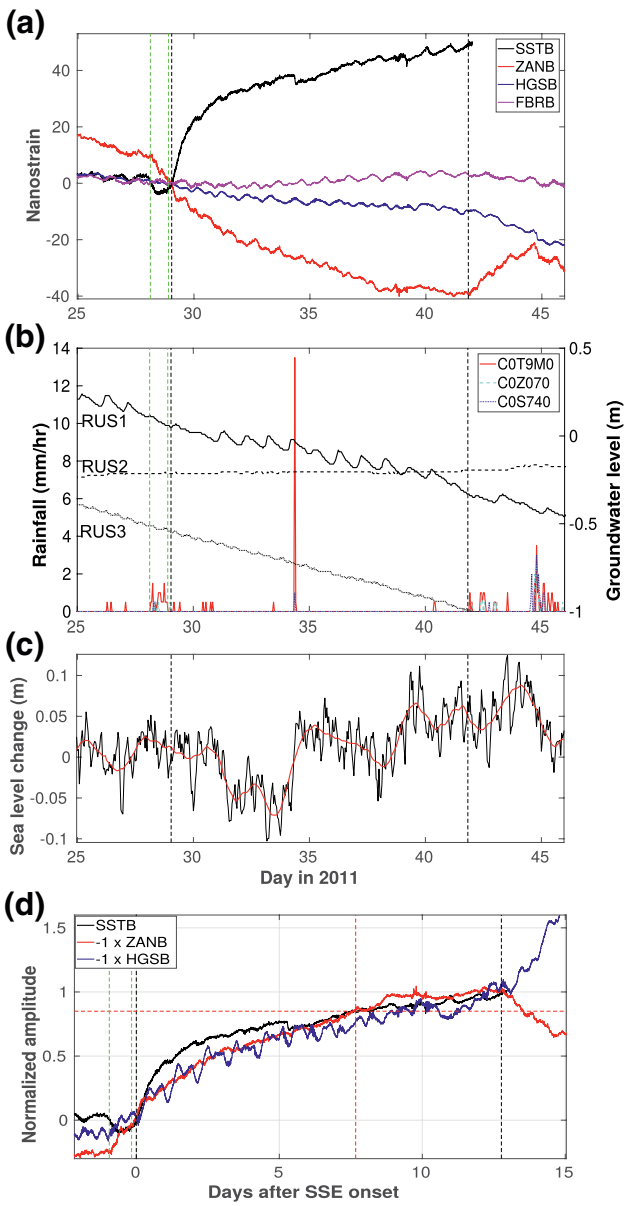

Figure 2. (a) Residual dilatation signals (expansion strain > 0). SSNB experiences a power outage from days 42–47. Vertical black and green dashed lines indicate the SSE episode duration (around days 29.06–41.8) and the light rainfall period preceding the SSE, respectively. (b) Hourly rainfall and groundwater level variations (black curves), and (c) detided sea level variations (black curve) and smoothed signal (red curve). (d) Dilatation signals from 27 January to 13 February 2011 (days 27–44) normalized by the value reached at the end of the slow slip event (SSE) episode (ZANB and HGSB are inverted). Vertical red dashed line indicates the timing of repeaters, occurring when 85% of total aseismic slip was relieved (4.25 cm) (horizontal red dashed line).

2. Near-Fault Instrumentation and Data Processing

Beginning in 2003, to shed additional light on the nature of the deformation in the LV, the Institute of Earth Sciences (IES) Academia Sinica, in cooperation with the Department of Terrestrial Magnetism, Carnegie Institution of Washington, has deployed 11 *Sacks-Evertson* (Sacks et al., 1971) borehole strainmeters along the LVF (Figure 1). They monitor rock volume change (dilatation ϵ_v) and complement the GPS measurements for detecting crustal transients at short to intermediate periods (minutes to weeks). We calibrate the dilatometers using solid-Earth and ocean tides (Canitano et al., 2018b) (Figure S1), and correct the strain data for borehole relaxation, for solid-Earth and ocean tidal strain and air pressure induced strain. To monitor strain changes caused by hydrological variations, rainfall and groundwater level stations were deployed by the Central Weather Bureau (CWB) and the Water Resources Bureau in Taiwan, respectively. Sea level changes are continuously monitored by a tide-gauge installed near Chengkung and operated by the CWB. The corrected strain signals and environmental signals are presented in Figure 2. We process the GPS data (Figure 1b) with the GAMIT10.42/GLOBK5.16 software packages (Herring et al., 2010) using the 2005 International Terrestrial Reference Frame (ITRF2005) (Altamini et al., 2007) coordinates in GLOBK processing (Figure S2).

3. Detection and Characterization of the SSE

Volumetric strain response to rainfall represents the largest signal observed in strainmeter time-series. Hours to days following the rainfall, a contraction signal proportional to the amount of cumulative rainfall is recorded (Figure S3a). A rainfall-strain admittance of −0.51 nϵ/mm is found for the central LV (Hsu et al., 2015). At longer periods (weeks to months), an alternance of phases of contraction and expansion is observed, which suggests that volumetric crustal strain is likely modulated by the cumulative rainfall loading (Figure S3b). Such deformation is complex, highly site-dependent (e.g., local topography, rock elastic/poroelastic properties) (Mouyen et al., 2017), and its mechanisms remain poorly constrained in the region.

Starting on 29 January 2011 (day 29), we observe an expansion of +50 nanostrain (nϵ) at SSTB station, synchronous with a contraction of −39 nϵ at ZANB station and a moderate contraction (approximately −10 nϵ) at HGSB station (Figure 2a). FBRB does not record any relevant signal (SSNB and CHMB experience a power outage). On day 28.2, a light rainfall episode (12 mm of rainfall within 12 h) (Figures 2b and S4) occurs in the CR (Figure 1b, station C0T9M0 near ZANB) inducing a contraction of −7 nϵ at ZANB, which is about the value expected based on the rainfall-strain admittance in the region (Hsu et al., 2015). Rainfall has likely stopped when SSTB signal initiates its large expansion (Figure S4a), that is unlikely to be the strain response to rainfall. Besides, to produce the contraction detected by ZANB and HGSB (−39 nϵ and −10 nϵ, respectively), it would require continuous rainfall from days 29–42 with an amount of ∼80 mm and of 20 mm of water, respectively, which is not observed (Figure S4b). Therefore, strain variations are not associated with precipitation and neither are they induced by hydrology as no transient change in groundwater level is detected during January–February 2011 (Figure 2b). There are also no appreciable sea level changes, the largest variations occurring during day 34

(~0.1 m) and remain undetected by near-coastal stations (Figure 2c). Finally, no signal is detected by the GPS stations (Figure S2).

Strain signals with nearly similar temporal evolution are detected from days 29–41.8 in two networks distant by 35 km (Figure 2d). They are unrelated to environmental changes and represent unambiguous evidence for a slow slip episode. Signals follow a logarithmic time-dependence, a pattern observed on borehole strainmeters during a previous SSE (Canitano et al., 2019). Additionally, following day 41.8, ZANB records a moderate expansion (+20 nϵ) during 3 days (Figure 2a), while a contraction of approximately −5 nϵ is expected due to 10 mm of cumulative rainfall (Figure S4, station C0T9M0). HGSB records a contraction of −10 nϵ that is about five times larger than the expected changes due to 3–4 mm of rainfall (Figure S4, station C0Z070), while FBRB does not record any variation. Since these variations are unrelated to environmental perturbations or to sensor drift or relaxation, they may be the signature of a propagating source (e.g., Linde et al., 1996). However, it remains difficult to characterize this possible second slow phase because of the lack of data (no signal for SSTB), which limits our ability to fully decipher the complexity of this event. Consequently, we only characterize the 13-day long main phase and thus estimate a minimum moment magnitude for the sequence.

We search for a source compatible with the LVF (strike = 23°NE) and a geologic rake of 70°, which corresponds to the mean slip vector direction in the Yuli-Fuli region (Peyret et al., 2011). We estimate the optimal source location and magnitude for a rectangular fault with uniform slip embedded in an elastic homogeneous half-space (Okada, 1992) with a rigidity $G = 30$ GPa using a grid search approach derived from GPS source modeling (J. T. Lin et al., 2019) (Text S1 and Figure S5). A minimum misfit is achieved (rms < 1 nϵ) for a source with length of $L = 16$–24 km, width of $W = 3.8$–12 km and aseismic slip of $U = 2$–10 cm at the depth of 10.5–11.5 km. The fault surface is constrained in the range 65–288 km^2, the source aspect ratio (L/W) is ranging from 1.8 to 4.6 and the geodetic moment magnitude $M_w = 5.41$–5.45 (Figure S6a). Our preferred source model (rms misfit = 0.36 nϵ) is located at 10.75 km depth, it has length and width of 19 km × 6.4 km, respectively, and a total displacement of 5 cm ($M_w = 5.44$) (Figure S6b). The SSE geodetic moment magnitude is strongly constrained, it represents a typical value for a 2-week long SSE (Bürgmann, 2018; Michel et al., 2019) and agrees with an earthquake-like cubic moment-duration scaling, as reported in Cascadia (Dal Zilio et al., 2020; Michel et al., 2019) and Mexico (Frank & Brodsky, 2019). We compute the static stress drop $\Delta\sigma$ following Kanamori and Anderson (1975):

$$\Delta\sigma = \frac{8}{3\pi}\frac{GU}{\sqrt{LW}} \tag{1}$$

The average stress drop ranges from 0.03 to 0.32 MPa with $\Delta\sigma = 0.115$ MPa for our best source model, which is consistent with values from Gao et al. (2012).

We search for recurrent events for the 2004–2019 period using a geodetic template matching (e.g., Rousset et al., 2017) but found no additional events (Text S2 and Figure S7). At the minimum, the recurrence time of such event is about 7–8 years. Our search is however limited by the strain templates allowing to detect only events with nearly similar duration and location as the 2011 SSE. We cannot exclude either that our method failed to detect recurrent events with lower magnitude. Indeed, such signals are below the GPS ambient noise level and frequent rainfall strongly impact strainmeter records, potentially concealing transient signals.

4. Analyze of the Seismicity During the SSE Episode

We analyze the seismicity from days 28–43 in 2011 but find no evidence for the occurrence of nonvolcanic tremors or for a temporary increase in seismicity (Figure S8). We also search for repeating earthquakes (REs), as a possible seismological signature of aseismic slip (Uchida & Bürgmann, 2019). They represent nearly identical asperities that rupture repeatedly under the influence of aseismic slip (e.g., Beeler et al., 2001). We calculate the cross-correlation coefficients (ccc) of the vertical velocity signals for all earthquake pairs (13 events) recorded by 10 broadband seismic stations distant from 5 to 65 km from the SSE source (Figure 1a). We filter the 100-Hz sampling signals between 3 and 20 Hz to suppress microseismic noise and select a

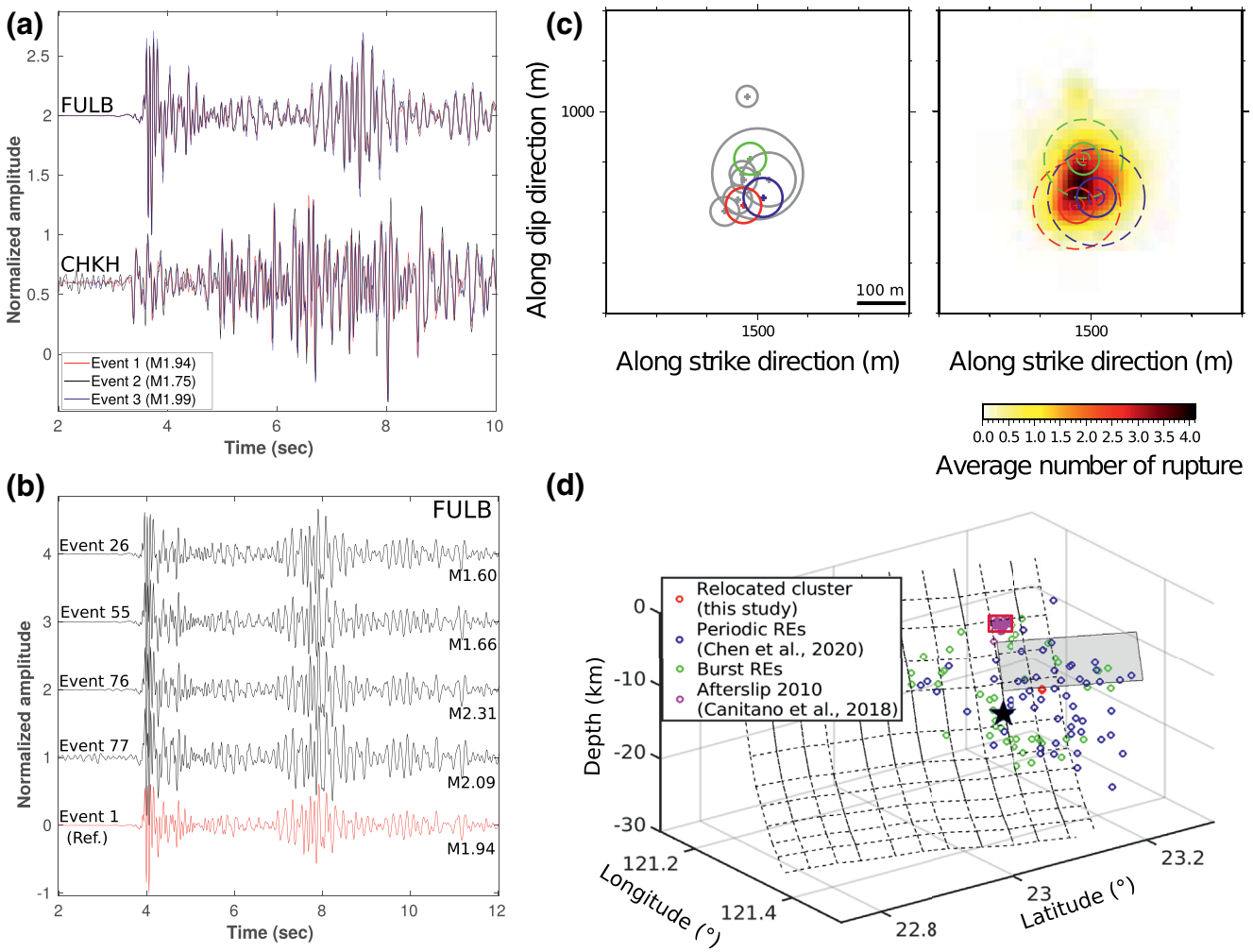

Figure 3. (a) Burst-type REs identified during the SSE episode (ccc > 0.92). (b) Multiplets (ccc > 0.90) detected during the 2003–2019 period for station FULB using template matching analysis. (c) Projection of the event centroids and rupture surfaces onto the LVF plane. (left) Mean source rupture radii. Red, green and blue circles denote events 1, 2, and 3 in 2011, respectively. Gray circles are other events of the multiplet. (right) Mean (plain circle) and extremum source radius uncertainties (dashed circles) for the 2011 events superimposed with the average number of ruptures of the multiplet. (d) Seismic and aseismic processes near the 2003 Chengkung earthquake (black star) source region. Periodic REs and burst-type REs are events with $M_L \geq 2$ for the 2000–2011 period (see Chen et al., (2020) for details). Gray and plain red rectangles outline the SSE and afterslip (Canitano et al., 2018a) fault planes, respectively. LVF, Longitudinal Valley Fault; RE, repeating earthquake, SSE, slow slip event.

cross-correlation window which includes *P*- and *S*-wave arrivals. Window lengths are ranging from 4 to 13 s between nearby and remote stations. We find high waveform coherence for three events (ccc > 0.92) (Figure 3a). They occur during a 40-min period on 5 February 2011 (day 36) and have local magnitude $M_L < 2$ (events 1–3, Table S2).

To further characterize the earthquake multiplet, we search for additional events for the 2003–2019 period using waveform template matching. We use event 1 as a template and perform sliding-window cross correlations (Yang et al., 2009) for the same previous stations and same *P*-*S* phase time-windows. A new event is added to the multiplet if its ccc with event 1 is ≥0.80, at minimum, for three stations. We find a total of 11 new events (Table S2 and Figure 3b) with $M_L = 1.43$–2.90. The multiplet is relocated using the double-difference algorithm *HypoDD* (Waldhauser & Ellsworth, 2000) with manually picked *P*- and *S*-wave absolute arrival times and relative cross-correlation delay times. The relative times are determined by cross-correlating all earthquake pairs in the multiplet for both *P* and *S* waves using 2-s length windows beginning 0.1 s before manual wave picks. All pairs satisfying ccc ≥ 0.80 are retained for the inversions (85 pairs). To ensure a good

constraint on the absolute location of the multiplet, we jointly relocate it with 100 earthquakes selected near and within the SSE source. For these earthquakes, only manually picked *P*- and *S*-arrival times are inverted.

As a result, 10 events of the multiplet (M_L = 1.43–2.76) are relocated at the depth of about 14.2 km along a structure dipping about 55° southeastward (Figure S9), which is compatible with the geometry of the LVF. We assess the relative location uncertainties by a bootstrap resampling method following Waldhauser and Ellsworth (2000) for two types of uncertainties. First we assess the relative uncertainty inside the multiplet by bootstrapping residual times from the relocation of the multiplet without the additional earthquakes. Second is absolute uncertainty of the multiplet location estimated from the bootstrapping performed on the joint relocation. We obtain relative errors of about 24, 19, and 42 m in E-W, N-S, and vertical directions, and absolute errors of 178, 124, and 243 m in E-W, N-S, and vertical directions, respectively (Figure S10). The source radius R of each relocated event is estimated based on the relationship between stress drop $\Delta\sigma$ and seismic moment M_0 (Eshelby, 1957). Local magnitude M_L is converted to moment magnitude M_w using an empirical formula derived for Taiwan (Huang et al., 2000; Wu et al., 2005) and M_0 is estimated from M_w following Kanamori and Anderson (1975) (Text S3). Source radii range between 20 and 90 m (30–40 m for the 3 events in 2011) with uncertainties varying between −40 and +250%. Then, using a stochastic approach, we find a maximum of four cumulative ruptures inside the cluster, suggesting limited source overlapping and an asperity that likely ruptured by small parts (Figure 3c).

5. Influence of Static Stress Changes From the 2003 Chengkung Earthquake

The SSE source is adjacent to the rupture area of the 2003 M_w 6.8 Chengkung earthquake. The mainshock was followed by an afterslip with an aseismic moment equivalent to 0.8 times the seismic moment at the end of the study period (end of November 2010) (Thomas, Avouac, Champenois, et al., 2014; Thomas et al., 2017). The SSE occurred two months after the end of the study period while some parts of the fault were still creeping at higher rate than during the preseismic period (Thomas, Avouac, Champenois, et al., 2014; Thomas et al., 2017). Given that SSEs are highly sensitive to small stress perturbations (a few kPa) (e.g., Hawthorne & Rubin, 2010), we estimate the contribution of coseismic and postseismic slip to the SSE occurrence using the Coulomb failure criterion. If $\delta\sigma_n$ and $\delta\tau$ represent respectively the changes in normal stress (tensile stress is positive) and shear stress on the fault plane (positive in the direction of the long-term fault slip) induced by the cumulative slip, the static Coulomb stress change δCFF is defined as:

$$\delta CFF = \delta\tau + \mu'\delta\sigma_n \tag{2}$$

where μ' is the effective friction coefficient, here taken as 0.4. The fault moves closer to failure if $\delta CFF > 0$ and away from failure if $\delta CFF < 0$. δCFF is resolved onto the LVF plane using *Coulomb 3.3* (Lin & Stein, 2004; Toda et al., 2005) for an assigned rake, we further argue for.

Unlike the simple geometry we use to compute the SSE source (justified by the strain data resolution), the fault geometry in the kinematic study followed the local variation of strike of the surface fault trace (to be consistent with the high InSAR spatial resolution) as well as the variation of the dip angle, highlighted by the microseismicity (Thomas, Avouac, Champenois, et al., 2014). Thus, even the projection onto the fault of a smooth displacement field leads to a corresponding rake that varies from one patch to another. It can therefore be misleading to compute the δCFF on each individual patch for an imposed rake corresponding to that of the SSE. We consequently plot the cumulative displacement as well as the δCFF along the direction of long-term displacement of the LVF. The latter is given by the projection onto the fault of the long-term displacement of the Central Range relative to the Coastal Range (Thomas, Avouac, Champenois, et al., 2014). This further allows to discuss if the SSE accommodates some slip deficit. For the sake of the discussion we also compute the δCFF for a patch corresponding to the inferred SSE source (70°).

The time-evolution of postseismic slip is modeled using 7 years of geodetic data following the mainshock (Thomas, Avouac, Champenois, et al., 2014). Thus, modeled δCFF represents a very close estimate of the static stress changes on the fault at the SSE onset timing but predicts the cumulative stress as if it had occurred instantaneously. It does not account for the complex interactions between fault plane patches that occurred over the postseismic period. The SSE source is located in an area of very low coseismic slip,

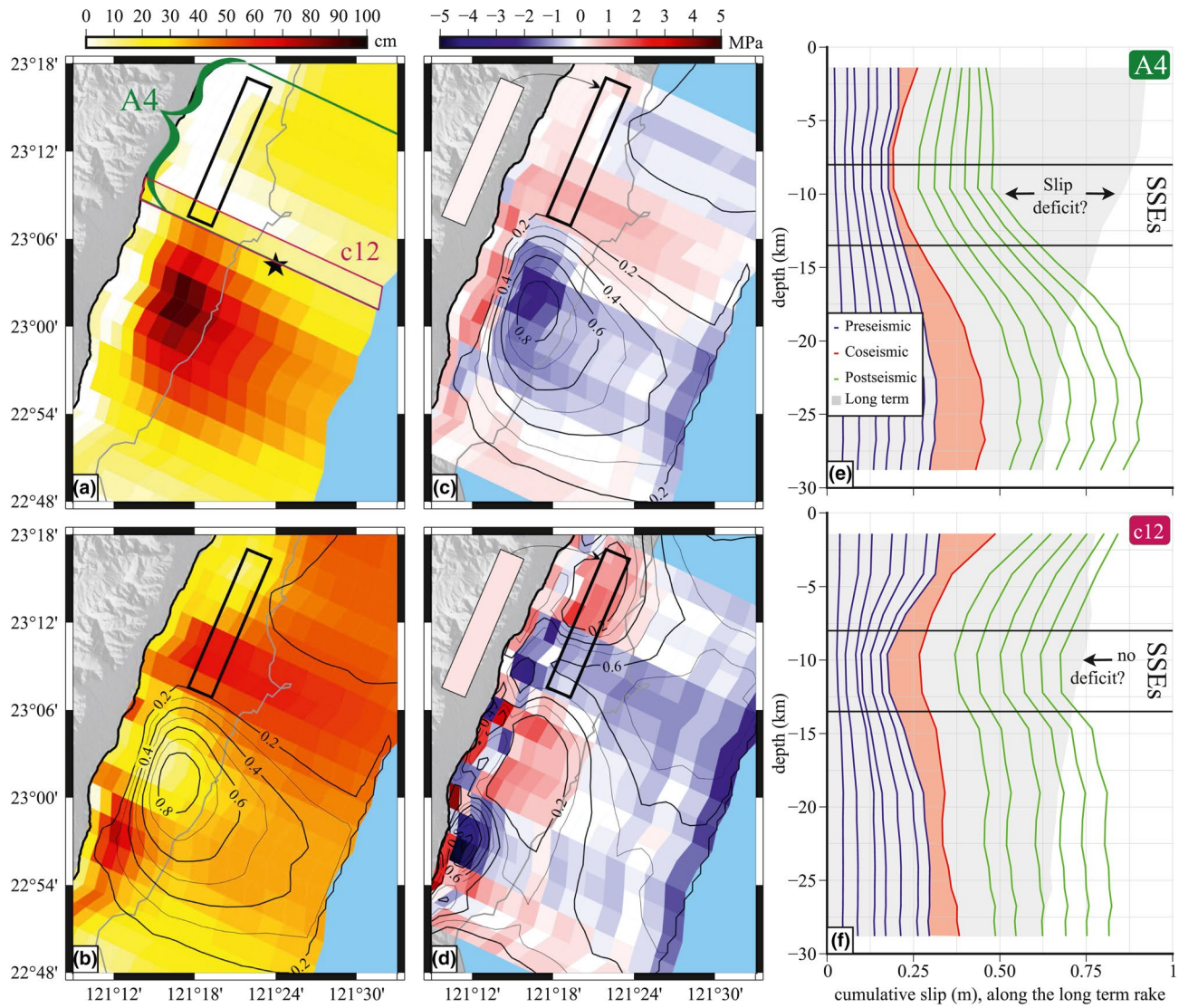

Figure 4. Kinematic slip models of (a) the 2003 Chengkung earthquake and (b) the following 7-year postseismic period (December 2003–November 2010). Static Coulomb stress changes imparted by (c) coseismic and (d) postseismic slip, resolved onto the LVF fault plane. The plane depicted on the side represents δCFF computed for a fixed rake of 70°. Black rectangle outlines the SSE rupture area and black star denotes the Chengkung earthquake epicenter. Black curves give the contour lines of the coseismic (b),(c) and postseismic (d) slip distribution models (in meter). Cumulative slip along the long-term rake for the A4 area and for the column c12 (see (a)) are given respectively in (e) and (f). For area A4, slip time-series are averaged for patches at the same depth, that is, we performed 15 times an along-strike average within a swath spanning seven patches (3.16 × 22.12 km). Cumulative slip with depth are plotted with an increment of 1 year for the 7-year preseismic (blue) and the 7-year postseismic (green) periods. Red and gray shading give respectively the coseismic slip and the total motion of the fault if it had crept at the long-term slip rate during those 14 years. LVF, Longitudinal Valley Fault; SSE, slow slip event.

≤0.1 m (Figure 4a), which results in positive Coulomb stress changes of 0.5–0.7 MPa, essentially in the southern SSE region (Figure 4c). Moderate cumulative postseismic slip (about 0.2–0.6 m during the 7-year period) (Figure 4b) is observed in the source region with significant positive ($\delta CFF \sim$ 0.5–0.7 MPa) and negative ($\delta CFF \sim -0.5$ MPa) Coulomb stress changes in the northern and southern SSE area, respectively (Figure 4d). Cumulative slip estimated for the preseismic period (January 1997–December 2003) is about 20–30 cm in the SSE source region (Figures 4e and S11c). It is however more subject to caution given that data are more sparse and as a direct consequence the applied smoothing is stronger (see Thomas, Avouac, Gratier, et al., 2014 for details), which inevitably impacts the δCFF computation. However, δCFF is essentially null and negative in the southern and central sections ($\delta CFF \sim -0.5$ MPa) and positive ($\delta CFF \sim$ 0.5 MPa) in a limited northermost section. Note that since Coulomb prestress changes are only estimated

over a 7-year period, they may represent a minimum amount in the SSE area at the onset of the Chengkung rupture. Finally, for a rake of 70° on the patch corresponding to the SSE source, $\delta CFF \sim 0.1$–0.2 MPa for all models (Figures 4c & d and S11d).

6. Discussion and Concluding Remarks

Coseismic static stress changes are permanent perturbations, with effects lasting from days to years (e.g., Segou & Parsons, 2020), and can therefore explain an extended period for triggering of aftershocks (King et al., 1994) and SSEs (Hayes et al., 2014; Rolandone et al., 2018). Besides, long-lasting stress effects from postseismic deformation can also play a significant role in promoting delayed rupture (Segou & Parsons, 2018). The 2017 M_w 7.1 Puebla earthquake, Mexico, was likely triggered by postseismic stress changes (up to 0.1 MPa) following the 2012 M_w 7.5 Oaxaca event (Segou & Parsons, 2018), while a combination of postseismic stress changes from the 1964 M_w 9.2 Alaska earthquake and a 12-year-long SSE possibly promoted the 2018 M_w 7.1 Anchorage earthquake (Segou & Parsons, 2020).

Here, the 2003 Chengkung earthquake represents the largest event impacting the LVF during the past decades. It generated maximum static Coulomb stress perturbations in the SSE source region two orders of magnitude larger than any other event (Figure S12). We propose that the SSE occurrence has been promoted by the significant Coulomb stress changes ($\delta CFF > 0.5$–1 MPa, about 5–10 times greater than the SSE average stress drop) imparted by a combination of coseismic and postseismic slip from the earthquake, and which persists several years after the mainshock. δCFF distribution onto the SSE fault plane reveals a complex pattern (Figure 4 and S11). First, the preseismic stress (1997–2003) is essentially negative, with a minimum level similar to the positive coseismic δCFF. Therefore, it is possible that coseismic Coulomb stress changes could not overwhelm Coulomb prestress (e.g., Mildon et al., 2019), which may explain the lack of detected recurrent SSEs right after the mainshock, despite the favorable stress conditions. Conversely, we simply missed an event since no strain data are available within 6 months following the mainshock. Then, the positive coseismic δCFF on the southern part of the SSE area may have induced the postseismic slip (0.4–0.6 m) which in turn generated significant Coulomb stress changes ($\delta CFF > 0.5$ MPa) in the northern section. The latter could be the trigger of the SSE. However, δCFF only gives the relative changes of stress for a defined time interval, here the 7-year preseismic, coseismic, and 7-year postseismic periods.

We now analyze the location of the SSE with respect to the total slip budget using Thomas, Avouac, Gratier, et al. (2014) kinematic study. We plot the along-dip variations of slip through time, at the SSE latitude (Figure 4e, area A4) and compare the accumulated slip over ~14 years with the total motion of the fault if it had crept at the long-term slip rate. We observe a slip deficit between 0 and 16 km depth, which encompasses the SSE source area. Analyzing the along-strike variation of slip within area A4, we see that for the southernmost section (column c12, Figure 4f), there is almost no slip deficit unlike for the columns c13 to c18 (Figures S13). Combining δCFF and the kinematic analysis we propose the following scenario: 7 years of afterslip leads to a $\delta CFF > 0$ in the north, which triggers the SSE. It then propagates southward and was further stopped by a stress barrier, that is, an area where all the stress has been released by a combination of coseismic and postseismic slip. We also observe a slip deficit near the surface (Figure 4e) which is not covered by the inferred SSE source model. We still know little about the physical mechanisms and conditions that lead to SSE generation near the surface, where deformation is more distributed (Thomas, Avouac, Champenois, et al., 2014). Thus, while most of the deformation occurs on the LVF, we could have failed to detect slip on secondary faults, underestimating the deformation near the surface, therefore leading to an apparent slip deficit. This is supported by the evidence that the shallow creeping portion of the fault (at the depths < 7 km) had acted as a rather effective barrier during the 2003 seismic rupture (Thomas et al., 2017). This means that no remaining stress (therefore no slip deficit) was available to help the rupture propagates to the surface. These observations raise the question of the role of the SSE transient zone during the 2003 Chengkung rupture. Since insignificant coseismic slip is inferred in the transient region (Figure 4 and S13), the latter may have acted as a barrier, limiting the rupture propagation northeastward. Rupture penetration in transient regions being mainly controlled by effective stress differences between "fast" and "slow" slip regions (J. T. Lin et al., 2020), further analysis are needed to decipher whether a dominant aseismic slip mode prevails throughout the earthquake cycle for the transient slow slip zone (e.g., Perfettini et al., 2010;

Rolandone et al., 2018) (i.e., a permanent barrier), or if seismic ruptures can partially or completely penetrate it (e.g., J. T. Lin et al., 2020). Finally, the SSE region also lies in an area of moderate afterslip, suggesting that sections of the LVF experiencing afterslip can also host SSEs (Rolandone et al., 2018; Yarai & Ozawa, 2013).

In addition to triggering aseismic slip, the Chengkung earthquake had also impacted the dynamics of repeater sequences along the LVF, notably halving their recurrence interval (Y. Chen et al., 2020). During the 2011 SSE, we observe burst-type of nearly identical REs which are events that have extremely short recurrence intervals (Igarashi et al., 2003; Templeton et al., 2008). However, 8 events (out of 10) of the cluster have $M_L < 2$ for which distinguishing REs requires high-frequency signal contents and may remain poorly resolved in the seismic waveforms (Uchida & Bürgmann, 2019). Magnitude limitations as well as uncertainties on the source stress drops and relocations strongly limit our ability to resolve the source overlapping and to assess the source mechanisms of the REs. We therefore propose two possible scenario based on the previous analysis:

1. Since burst-type REs tend to occur off the major fault planes (Igarashi et al., 2003; Templeton et al., 2008) and Coulomb stress changes caused by the SSE in the RE region is negative ($\delta CFF \sim -0.1$ MPa) (Figure S14), the REs may have occurred spontaneously with no mechanical link with the SSE. Besides, no SSE is detected during other RE occurrences, and particularly during other burst-type REs (Figure S15), suggesting that aseismic slip is unlikely to be the dominant mechanism of REs in the region (K. H. Chen et al., 2009, 2020) (Figure 3d)
2. Conversely, since the fault plane solution of the REs is unknown, our Coulomb stress model, which consider the LVF as receiver fault, may not be adequate. Moreover, given the uncertainties on the RE relocations (Section 4) and that our best SSE source locations are within a range of a kilometer (Text S1), aseismic and seismic sources can be spatially colocated. This clustering may suggest a dominant control of the SSE on the repeating microearthquakes. However, given that source overlapping is not observed, the 40-min RE burst is unlikely to be the result of recurrent seismic ruptures to accommodate aseismic slip in the surrounding area (e.g., Beeler et al., 2001). It rather suggests a triggering cascade of ruptures (e.g., Lengliné & Marsan, 2009), in which event 1, likely triggered by aseismic slip, has then ruptured close-by, but distinct, asperities (as events 2 and 3), together partially rupturing the main asperity (event 54). Overall, burst-type REs are likely caused by local, transient stress concentration from nearby earthquakes and/or aseismic slip events (Templeton et al., 2008) and they are also observed during postseismic slip on the LVF (Canitano et al., 2018a)

To conclude, while a SSE was detected at the transition between the creeping section of the LVF and the locked zone (Canitano et al., 2019), we now show that the fault can also host larger events at seismogenic depths. A limited fraction (about 15%–35%) of ~0.15–0.35 m of the slip deficit accumulated in 2011 (Figure 4e) has been accommodated by the SSE, additional and/or recurrent aseismic transient slip should likely help to release the remaining slip deficit. Besides, the SSE region, which coincides with a region of low interseismic coupling (ISC ~ 0.1–0.3) (Figure S11b), is adjacent to the highly coupled Chengkung rupture region (ISC > 0.6). Future studies focusing on a systematic analyze of aseismic slip events and microseismicity combined with dynamic modeling of seismic-aseismic interactions through the seismic cycle would help to further interpret the complex deformation processes in the region, to identify areas with high seismic hazard, and to connect SSEs to large, destructive earthquakes (e.g., Radiguet et al., 2016).

Acknowledgments
We are grateful to Associate Editor German Prieto and two anonymous reviewers for their constructive suggestions and comments allowing to improve the manuscript. We thank Alan Linde, Selwyn Sacks and the support staff of the Carnegie Institution of Washington for the construction, installation, and maintenance of the dilatometers, and Hsin-Ming Lee for collecting the strainmeter data. The authors acknowledge Yi-Chuen Tsai and Mei-Jun Yu for processing the GPS data and Ya-Ju Hsu for providing codes for visualizing seismicity. We are grateful to Kate Chen and Yaochieh Chen for providing the repeater catalog. We thank Wen-Tzong Liang and Wen-Hui Lee for the access to the seismological data. This research is supported by the Ministry of Science and Technology grant MOST 108-2116-M-001-027-MY2. This is the contribution of the Institute of Earth Sciences, Academia Sinica, IESAS2386.

Data Availability Statement

Some figures were drawn using the Generic Mapping Tools (Wessel & Smith, 1998). Strainmeter, hydrological, tide-gauge and broadband seismological data (CWB and BATS network [Institute of Earth Sciences, Academia Sinica, Taiwan, 1996]) are archived in PANGAEA (https://issues.pangaea.de/browse/PDI-25970).

References

Altamini, Z., Collilieux, X., Legrand, J., Garayt, B., & Boucher, C. (2007). ITRF2005: A new release of the International Terrestrial Reference Frame based on time series of station positions and Earth Orientation Parameters. *Journal of Geophysical Research*, *112*, B09401. https://doi.org/10.1029/2007JB004949

Barrier, E., & Angelier, J. (1986). Active collision in eastern Taiwan: The coastal range. *Tectonophysics*, *125*, 39–72.

Beeler, N. M., Lockner, D. A., & Hickman, S. H. (2001). A simple stick-slip and creep slip model for repeating earthquakes and its implication for micro-earthquakes at Parkfield. *Bulletin of the Seismological Society of America*, *91*, 1797–1804.

Beroza, G. C., & Ide, S. (2011). Slow earthquakes and nonvolcanic tremors. *Annual Review of Earth and Planetary Sciences*, *39*, 271–296.

Bürgmann, R. (2018). The geophysics, geology and mechanics of slow fault slip. *Earth and Planetary Science Letters*, *495*, 112–134.

Canitano, A., Godano, M., Hsu, Y. J., Lee, H. M., Linde, A. T., & Sacks, S. (2018a). Seismicity controlled by a frictional afterslip during a small magnitude seismic sequence ($M_L < 5$) on the Chihshang Fault, Taiwan. *Journal of Geophysical Research: Solid Earth*, *123*, 2003–2018. https://doi.org/10.1002/2017JB015128

Canitano, A., Hsu, Y. J., Lee, H. M., T Linde, A., & Sacks, S. (2018b). Calibration for the shear strain of 3-component borehole strainmeters in eastern Taiwan through Earth and ocean tidal waveform modeling. *Journal of Geodesy*, *92*(3), 223–240.

Canitano, A., Gonzalez-Huizar, H., Hsu, Y. J., Lee, H. M., Linde, A. T., & Sacks, S. (2019). Testing the influence of static and dynamic stress perturbations on the occurrence of a shallow, slow slip event in eastern Taiwan. *Journal of Geophysical Research: Solid Earth*, *124*, 3073–3087. https://doi.org/10.1029/2018JB016742

Chen, K. H., Rau, R. J., & Hu, J. C. (2009). Variability of repeating earthquake behavior along the Longitudinal Valley fault zone of eastern Taiwan. *Journal of Geophysical Research*, *114*, B05306. https://doi.org/10.1029/2007JB005518

Chen, Y., Chen, K. H., Hu, J. C., & Lee, J. C. (2020). Probing the variation in aseismic slip behavior around an active suture zone: Observations of repeating earthquakes in Eastern Taiwan. *Journal of Geophysical Research: Solid Earth*, *125*, e2019JB018561 https://doi.org/10.1029/2019JB018561

Dal Zilio, L., Lapusta, N., & Avouac, J. P. (2020). Unraveling scaling properties of slow-slip events. *Geophysical Research Letters*, *47*, e2020GL087477. https://doi.org/10.1029/2020GL087477

Eshelby, J. D. (1957). The determination of the elastic field of an ellipsoid inclusion and related problems. *Proceedings of the Royal Society of London A*, *241*, 376–396.

Fasola, S. L., Brudzinski, M. R., Holtkamp, S. G., Graham, S. E., & Cabral-Cano, E. (2019). Earthquake swarms and slow slip on a sliver fault in the Mexican subduction zone. *Proceedings of the National Academy of Sciences of the United States of America*, *116*(15), 7198–7206.

Frank, W. B., & Brodsky, E. E. (2019). Daily measurement of slow slip from low-frequency earthquakes is consistent with ordinary earthquake scaling. *Sciences Advances*, *5*(10), eaaw9386.

Gao, H., Schmidt, D. A., & Weldon, R. J. (2012). Scaling relationships of source parameters for slow slip events. *Bulletin of the Seismological Society of America*, *102*(1), 352–360.

Gualandi, A., Nichele, C., Serpelloni, E., Chiaraluce, L., Latorre, D., Belardinelli, M. E., & Avouac, J. P. (2017). Aseismic deformation associated with an earthquake swarm in the northern Apennines (Italy). *Geophysical Research Letters*, *44*, 7706–7714. https://doi.org/10.1002/2017GL073687

Hawthorne, J. C., & Rubin, A. M. (2010). Tidal modulation of slow slip in Cascadia. *Journal of Geophysical Research*, *115*, B09406. https://doi.org/10.1029/2010JB007502

Hayes, G. P., Furlong, K. P., Benz, H. M., & Herman, M. W. (2014). Triggered aseismic slip adjacent to the 6 February 2013 M_w 8.0 Santa Cruz Islands megathrust earthquake. *Earth and Planetary Science Letters*, *388*, 265–272.

Herring, T., King, W., & McCluskey, S. M. (2010). *Introduction to GAMIT/GLOBK release 10.4*. Cambridge: Massachusetts Institute of Technology.

Hsu, Y. J., Chang, Y. S., Liu, C. C., Lee, H. M., Linde, A. T., Sacks, S., et al. (2015). Revisiting borehole strain, typhoons, and slow earthquakes using quantitative estimates of precipitation-induced strain changes. *Journal of Geophysical Research: Solid Earth*, *120*, 4556–4571. https://doi.org/10.1002/2014JB011807

Huang, K. C., H. Kao and Y. M. Wu (2000), *The determination of ML-Mw in Taiwan*. Paper presented at 8th Annual Meeting of Geophysical Society of China, Taipei City, Taiwan, pp. 193–201.

Igarashi, T., Matsuzawa, T., & Hasegawa, A. (2003). Repeating earthquakes and interplate aseismic slip in the northeastern Japan subduction zone. *Journal of Geophysical Research*, *108*(B5), 2249. https://doi.org/10.1029/2002JB001920

Institute of Earth Sciences, Academia Sinica, Taiwan (1996). *Broadband array in Taiwan for seismology*. Taiwan: Institute of Earth Sciences, Academia Sinica. Other/seismic network. https://doi.org/10.7914/SN/TW

Kanamori, H., & Anderson, D. L. (1975). Theoretical basis of some empirical relation in seismology. *Bulletin of the Seismological Society of America*, *65*(5), 1073–1095.

King, G. C. P., Stein, R. S., & Lin, J. (1994). Static stress changes and the triggering of earthquakes. *Bulletin of the Seismological Society of America*, *84*(3), 935–953.

Lee, J. C., Angelier, J., Chu, H. T., Hu, J. C., Jeng, F. S., & Rau, R. J. (2003). Active fault creep variations at Chihshang, Taiwan, revealed by creep meter monitoring, 1998-2001. *Journal of Geophysical Research*, *108*(B11), 2528. https://doi.org/10.1029/2003JB002394

Lengliné, O., & Marsan, D. (2009). Inferring the coseismic and postseismic stress changes caused by the 2004 $M_w = 6$ Parkfield earthquake from variations of recurrence times of microearthquakes. *Journal of Geophysical Research*, *114*, B10303. https://doi.org/10.1029/2008JB006118

Lin, J. T., Chang, W. L., Melgar, D., Thomas, A. M., & Chiu, C. Y. (2019). Quick determination of earthquake source parameters from GPS measurements: a study of suitability for Taiwan. *Geophysical Journal International*, *219*, 1148–1162.

Lin, J. T., Aslam, K. S., Thomas, A. M., & Melgar, D. (2020). Overlapping regions of coseismic and transient slow slip on the Hawaiian décollement. *Earth and Planetary Science Letters*, *544*, 116353. https://doi.org/10.1016/j.epsl.2020.116353

Linde, A. T., Gladwin, M. T., Johnston, M. J. S., Gwyther, R. L., & Bilham, R. G. (1996). A slow earthquake sequence on the San Andreas fault. *Nature*, *383*, 65–68.

Lin, J., & Stein, R. S. (2004). Stress triggering in thrust and subduction earthquakes and stress interaction between the southern San Andreas and nearby thrust and strike-slip faults. *Journal of Geophysical Research*, *109*, B02303. https://doi.org/10.1029/2003JB002607

Liu, C. C., Linde, A. T., & Sacks, I. S. (2009). Slow earthquakes triggered by typhoons. *Nature*, *459*, 833–836.

Michel, S., Gualandi, A., & Avouac, J. P. (2019). Similar scaling laws for earthquakes and Cascadia slow-slip events. *Nature*, *574*, 522–526. https://doi.org/10.1038/s41586-019-1673-6

Mildon, Z. K., Roberts, G. P., Faure Walker, J. P., & Toda, S. (2019). Coulomb pre-stress and fault bends are ignored yet vital factors for earthquake triggering and hazard. *Nature Communications*, *10*, 2744. https://doi.org/10.1038/s41467-019-10520-6

Mouyen, M., Canitano, A., Chao, B. F., Hsu, Y. J., Steer, P., Longuevergne, L., & Boy, J. P. (2017). Typhoon-induced ground deformation. *Geophysical Research Letters*, *44*(21) 11004–11011.

Murase, M., Matta, N., Lin, C. H., Chen, W. S., & Koizumi, N. (2013). An episodic creep-slip event detected by precise levelling surveys in the central part of the Longitudinal Valley Fault, eastern Taiwan, in 2011-2012. *Tectonophysics*, *2013*, 904–913.

Okada, Y. (1992). Internal deformation due to shear and tensile faults in a half-space. *Bulletin of the Seismological Society of America*, *82*(2), 1018–1040.

Peng, Z., & Gomberg, J. (2010). An integrated perspective of the continuum between earthquakes and slow-slip phenomena. *Nature Geoscience*, *3*, 599–607. https://doi.org/10.1038/NGEO940

Perfettini, H., Avouac, J. P., Tavera, H., Kositsky, A., Nocquet, J. M., Bondoux, F., et al. (2010). Seismic and aseismic slip on the Central Peru megathrust. *Nature*, *465*, 78–81.

Peyret, M., Dominguez, S., Cattin, R., Champenois, J., Leroy, M., & Zajac, A. (2011). Present-day interseismic surface deformation along the Longitudinal Valley, eastern Taiwan, from a PS-InSAR analysis of the ERS satellite archives. *Journal of Geophysical Research*, *116*, B03402. https://doi.org/10.1029/2010JB007898

Radiguet, M., Perfettini, H., Cotte, N., Gualandi, A., Valette, B., Kostoglodov, V., et al. (2016). Triggering of the 2014 M_w 7.3 Papanoa earthquake by a slow slip event in Guerrero, Mexico. *Nature Geoscience*, *9*, 829–833. https://doi.org/10.1038/NGEO2817

Rolandone, F., Nocquet, J. M., Mothes, P. A., Jarrin, P., Vallée, M., Cubas, N., et al. (2018). Areas prone to slow slip events impede earthquake rupture propagation and promote afterslip. *Science Advances*, *4*, eaao6596.

Rousset, B., Campillo, M., Lasserre, C., Frank, W. B., Cotte, N., Walpersdorf, A., et al. (2017). A geodetic matched filter search for slow slip with application to the Mexico subduction zone. *Journal of Geophysical Research: Solid Earth*, *122*. 10498–10514.

Sacks, S., Suyehiro, S., Evertson, D. W., & Yamagishi, Y. (1971). Sacks-Evertson strainmeter, its installation in Japan and some preliminary results concerning strain steps. *Papers in Meteorology and Geophysics*, *22*, 195–208.

Segou, M., & Parsons, T. (2018). Testing earthquake links in Mexico from 1978 to the 2017 $M = 8.1$ Chiapas and $M = 7.1$ Puebla shocks. *Geophysical Research Letters*, *45*, 708–714.

Segou, M., & Parsons, T. (2020). The role of seismic and slow slip events in triggering the 2018 M7.1 Anchorage earthquake in the South-central Alaska subduction zone. *Geophysical Research Letters*, *47*, e2019GL086640. https://doi.org/10.1029/2019GL086640

Templeton, D. C., Nadeau, R. M., & Bürgmann, R. (2008). Behavior of repeating earthquake sequences in Central California and the implications for subsurface fault creep. *Bulletin of the Seismological Society of America*, *98*(1), 52–65.

Thomas, M. Y., Avouac, J. P., Gratier, J. P., & Lee, J. C. (2014). Lithological control on the deformation mechanism and the mode of fault slip on the Longitudinal Valley Fault, Taiwan. *Tectonophysics*, *632*, 48–63.

Thomas, M. Y., Avouac, J. P., Champenois, J., Lee, J. C., & Kuo, L. C. (2014). Spatiotemporal evolution of seismic and aseismic slip on the Longitudinal Valley Fault, Taiwan. *Journal of Geophysical Research*, *119*(6), 5114–5139.

Thomas, M. Y., Avouac, J. P., & Lapusta, N. (2017). Rate-and-state friction properties of the Longitudinal Valley Fault from kinematic and dynamic modeling of seismic and aseismic slip. *Journal of Geophysical Research*, *122*, 3115–3137. https://doi.org/10.1002/2016JB013615

Toda, S., SteinRichards-Dinger, R. S. K., & Bozkurt, S. (2005). Forecasting the evolution of seismicity in southern California: Animations built on earthquake stress transfer. *Journal of Geophysical Research*, *110*, B05S16. https://doi.org/10.1029/2004JB003415

Uchida, N., & Bürgmann, R. (2019). Repeating earthquakes. *Annual Review of Earth and Planetary Sciences*, *47*, 305–332. https://doi.org/10.1146/annurev-earth-053018-060119

Vallée, M., Nocquet, J. M., Battaglia, J., Font, Y., Segovia, M., Régnier, M., et al. (2013). Intense interface seismicity triggered by a shallow slow slip event in the Central Ecuador subduction zone. *Journal of Geophysical Research*, *118*, 2965–2981.

Waldhauser, F., & Ellsworth, W. L. (2000). A double-difference earthquake location algorithm: Method and application to the northern Hayward fault. *Bulletin of the Seismological Society of America*, *90*(6), 1353–1368.

Wessel, P., & Smith, W. H. F. (1998). New, improved version of the Generic Mapping Tools released. *Eos, Transactions American Geophysical Union*, *79*, 579. https://doi.org/10.1029/98EO00426

Wu, Y. M., Allen, R. M., & Wu, C. F. (2005). Revised M_L determination for crustal earthquakes in Taiwan. *Bulletin of the Seismological Society of America*, *95*(6), 2517–2524.

Yang, H., Zhu, L., & Chu, R. (2009). Fault-plane determination of the 18 April 2008 Mount Carmel, Illinois, earthquake by detecting and relocating aftershocks. *Bulletin of the Seismological Society of America*, *99*(6), 3413–3420.

Yarai, H., & Ozawa, S. (2013). Quasi-periodic slow slip events in the afterslip area of the 1996 Hyuga-nada earthquakes, Japan. *Journal of Geophysical Research*, *118*, 2512–2527.

Yu, S. B., Chen, H. Y., & Kuo, L. C. (1997). Velocity field of GPS stations in the Taiwan area. *Tectonophysics*, *274*, 51–59.